A more accurate reconstruction system matrix for quantitative proton computed tomography

S. N. Penfold[a] and A. B. Rosenfeld
Centre for Medical Radiation Physics, University of Wollongong, Wollongong,
New South Wales 2522, Australia

R. W. Schulte
Department of Radiation Medicine, Loma Linda University Medical Center, Loma Linda, California 92354

K. E. Schubert
Department of Computer Science and Engineering, California State University,
San Bernardino, California 92407

An accurate system matrix is required for quantitative proton CT (pCT) image reconstruction with iterative projection algorithms. The system matrix is composed of chord lengths of individual proton path intersections with reconstruction pixels. In previous work, reconstructions were performed assuming constant intersection chord lengths, which led to systematic errors of the reconstructed proton stopping powers. The purpose of the present work was to introduce a computationally efficient variable intersection chord length in order to improve the accuracy of the system matrix. An analytical expression that takes into account the discrete stepping nature of the pCT most likely path (MLP) reconstruction procedure was created to describe an angle-dependent effective mean chord length function. A pCT dataset was simulated with GEANT4 using a parallel beam of 200 MeV protons intersecting a computerized head phantom consisting of tissue-equivalent materials with known relative stopping power. The phantom stopping powers were reconstructed with the constant chord length, exact chord length, and effective mean chord length approaches, in combination with the algebraic reconstruction technique. Relative stopping power errors were calculated for each anatomical phantom region and compared for the various methods. It was found that the error of approximately 10% in the mean reconstructed stopping power value for a given anatomical region, resulting from a system matrix with a constant chord length, could be reduced to less than 0.5% with either the effective mean chord length or exact chord length approaches. Reconstructions with the effective mean chord length were found to be approximately 20% faster than reconstructions with an exact chord length. The effective mean chord length method provides the possibility for more accurate, computationally efficient quantitative pCT reconstructions. © *2009 American Association of Physicists in Medicine*.
[DOI: 10.1118/1.3218759]

I. INTRODUCTION

In proton therapy, the maximum dose along the radiation path is deposited in a sharp peak at the end of the proton range, in what is known as the Bragg peak. To achieve dose conformality and thus healthy tissue sparing, the energy of the proton beam is adjusted so that the maximum proton range in the patient corresponds to the distal edge of the target volume. This approach requires accurate knowledge of the proton energy loss characteristics when the protons interact within the patient.

The majority of current proton treatment centers use pencil beam algorithms for treatment planning due to their computational efficiency.[1,2] In this approach, a pencil beam dose deposition model based on the experimentally measured or simulated depth-dose curves in water is convolved with a three-dimensional (3D) map of stopping power relative to water. Currently, the relative stopping powers are obtained by converting x-ray CT Hounsfield units via an empirically derived calibration curve.[3–5] This conversion leads to errors in the estimated proton range during treatment, typically on the order of 3% of the maximum proton range.[6] Thus, a combination of the errors inherent in the x-ray CT scan, and the errors arising from the empirically derived conversion function can contribute to a significant final range uncertainty in the proton treatment plan.

Proton CT (pCT) offers the possibility of directly obtaining the relative stopping power required for proton treatment planning calculations, removing the errors associated with x-ray CT and the conversion methods described above. In the current generation pCT design previously proposed by us,[7] individual protons in a parallel beam are tracked pre- and post-patient with 2D sensitive silicon strip detectors (SSDs), providing information about proton position and direction at

the boundaries of the image space. This allows the effects of multiple Coulomb scattering (MCS) within the object to be accounted for in a most likely path (MLP) estimation.[8] The advantage of this in terms of spatial resolution of the reconstructed image has been shown in a previous study.[9]

In addition to tracking the position of individual protons, the energy lost by each proton after traversal of the image space is recorded. Using these measurements, one can calculate either the path integral of relative electron density of a water equivalent object,[7] i.e., an object of water composition but varying electron density that produces the same energy loss as the real object, or the integral of relative stopping power along each proton path. Both quantities are equally applicable to pencil beam planning algorithms. In this study, we calculated the relative stopping power with

$$\int_L \rho_s(\mathbf{r}) dl = \int_{E_{\text{out}}}^{E_{\text{in}}} \frac{dE}{S(I_{\text{water}}, E)}. \tag{1}$$

Here, E_{in} and E_{out} are the measured entry and exit proton energies at the image space boundaries, respectively, ρ_s is the stopping power at spatial location $\mathbf{r}$ relative to water, and L is the estimated proton path through the image space. The stopping power in water $S(I_{\text{water}}, E)$ is given by the Bethe–Bloch equation,[10]

$$S(I_{\text{water}}, E) = \frac{4\pi r_e m_e c^2 N_{e,\text{water}}}{\beta^2(E)}$$
$$\times \left[\ln\left(\frac{2m_e c^2}{I_{\text{water}}} \frac{\beta^2(E)}{1 - \beta^2(E)} \right) - \beta^2(E) \right]. \tag{2}$$

In Eq. (2), r_e is the classical electron radius, m_e is the mass of the electron, $N_{e,\text{water}}$ is the electron density of water, β is the velocity of the proton relative to the speed of light c, and I_{water} is the mean excitation energy of water.

To generate images from the pCT data, iterative projection methods, e.g., the algebraic reconstruction technique (ART),[11] have been demonstrated as the preferred way of accommodating scattered proton paths.[9] Such methods are based on solving a system of equations of the form

$$\mathbf{A}\mathbf{x} = \mathbf{b}, \tag{3}$$

where the system matrix $\mathbf{A}$ is an $n \times m$ matrix whose elements a_j^i correspond to the length of intersection (chord length) of the i-th proton history's path with the j-th voxel, $\mathbf{x}$ is the unknown m-dimensional image vector, and $\mathbf{b}$ is the n-dimensional vector, whose elements b_i correspond to the integral relative stopping power measured along the i-th proton path [Eq. (1)].

In x-ray CT, the chord lengths of rays with individual pixels can be relatively easily calculated[12] due to the straight line nature of the radiation. This is not the case in pCT, where MCS deflects the proton path from a straight line. Our current approach to calculating the chord lengths in pCT has been to step through the image space in half-pixel step lengths and use the MLP formalism[8] to determine which pixels are intersected. These pixels are assigned constant chord lengths, equal to the pixel size, while pixels that are not
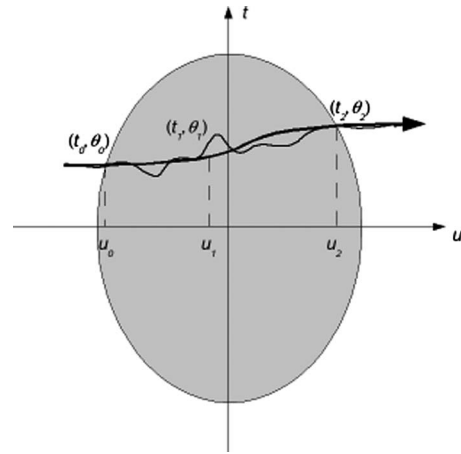
FIG. 1. Conceptual illustration of the MLP formalism. The bold line represents the MLP, while the faint line corresponds to a proton undergoing exaggerated multiple Coulomb scattering.

intersected are assigned a value of 0. We have observed that images reconstructed with this approach underestimated the relative stopping power of the imaged object by up to 13% when reconstructing with ART (unpublished data).

In the current work, two methods are described for determining the elements of the system matrix $\mathbf{A}$ more accurately. In the first method, exact chord lengths are calculated by joining MLP step points with straight line segments. In the second method, an analytical description of the mean chord length for a given proton path-reconstruction grid orientation is used to assign elements of the system matrix. The potential advantages of these approaches in quantitative pCT imaging are investigated by reconstructing a Monte Carlo generated pCT dataset with the ART algorithm. An assessment of the most valuable method is made based on quantitative image quality and reconstruction time.

II. METHODS

II.A. Most likely path formalism

As energetic protons traverse the object being imaged, individual trajectories deviate from straight line paths due to MCS. Our current pCT design includes position sensitive silicon strip detectors upstream and downstream of the object to record individual proton entry and exit positions and directions.[7] Using this information and Bayes theorem,[13] the MLP through the object can be calculated.[8]

Our MLP formalism makes use of the generalized Fermi–Eyges theory of MCS,[14] which accounts for proton energy loss in the scattering medium and employs a Gaussian scattering distribution. In this approach, the three-dimensional scattering is treated by projecting the path onto two orthogonal planes. The lateral displacement t and the projected 3D angle θ at the boundary locations, u_0 and u_2, are required for the evaluation of the MLP (Fig. 1). Given the entry and exit data vectors, $y_0 = (t_0, \theta_0)$ and $y_2 = (t_2, \theta_2)$, the most likely data vector at intermediate depth u_1 is calculated as[8]

$$y_{\text{MLP}} = (\Sigma_1^{-1} + R_1^T \Sigma_2^{-1} R_1)^{-1}(\Sigma_1^{-1} R_0 y_0 + R_1^T \Sigma_2^{-1} y_2). \tag{4}$$

In Eq. (4), Σ_1^{-1} and Σ_2^{-1} are the 2×2 inverse variance-covariance scattering matrices, R_0 and R_1 are the 2×2 translate-rotate matrices, and T denotes the matrix transpose operator. In our pCT reconstruction software, y_{MLP} is first calculated in half-pixel size increments along u assuming a $0°$ projection angle. Each MLP point is rotated by the current projection angle and the corresponding pixel or voxel number is recorded. Each pixel or voxel is then assigned a chord length.

II.B. Exact chord length approach

To calculate exact chord lengths with the MLP procedure, discrete step points were joined with straight line segments. In this work we set the step size to be equal to half the pixel size to ensure that in each step we either stay within the same pixel or move into one of the surrounding eight pixels. If the new step point was in the same pixel as the previous step, the Euclidian distance between the points was added to the chord length of the current pixel.

If the new step point was in one of the surrounding pixels that shares a boundary with the previous pixel, only one line of the reconstruction grid was crossed during the step. In this case the point of intersection of the straight line joining the step points and the appropriate grid line was calculated. The distance between the point of intersection and each step point was added to the corresponding pixel chord length.

If the new step point was in one of the surrounding pixels that share only a vertex with the previous pixel, two reconstruction grid lines were crossed during the step. In this case, the straight line joining the MLP step points was simultaneously solved with both of the grid lines forming the vertex of interest. These intersection points were used to calculate the chord lengths to be added to the previous and current pixel accordingly. Also, the distance between the intersection points was assigned to the intermediate pixel that was missed by the MLP stepping procedure.

II.C. Effective mean chord length approach

Calculation of individual step points with the MLP formalism is computationally expensive. To calculate exact chord lengths, a series of decisions and calculations must be made at each step point, adding to the pCT reconstruction time. We propose here a method that assigns a single chord length to all pixel intersections along a given proton path, speeding up the reconstruction. This approach is based on the assumption that a large number of protons will traverse the image grid with a given orientation and have a uniform spatial distribution. In this case, deterministic proton path-pixel intersections can be treated in a statistical manner. In this section, we derive the effective mean chord length function that describes this scenario, while taking the discrete stepping nature of the MLP into account.

While the majority of pixel intersections will be detected by the MLP calculation (i.e., when a step point occurs within the given pixel), the discrete stepping nature means that
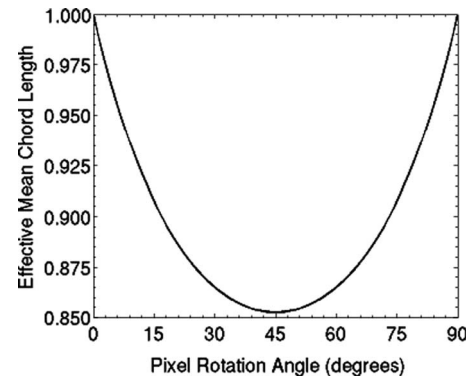
FIG. 2. Plot of the derived effective mean chord length as a function of pixel rotation angle.

some pixel intersections will be undetected. The effective mean chord length combines these two components. Firstly, to account for the pixel intersections that are detected by the MLP stepping process, we calculated the *mean detected chord length*. By considering a single representative pixel, this quantity was found by taking an average over all possible chord lengths for a given path-pixel orientation, weighted by the probability that a step point is registered along a given chord.

Secondly, to account for the undetected chords in the overall proton path length through the image space, a correction term was added to the mean detected chord length. This correction term is composed of the *mean undetected chord length* weighted by the probability that a step point does not occur inside a pixel. Combining these, the effective mean chord length is given as

$$\bar{\Delta}_{\text{eff}}(\theta) = \bar{\Delta}_d(\theta) + p_u(\theta)\bar{\Delta}_u(\theta). \tag{5}$$

Here, $\bar{\Delta}_{\text{eff}}$ is the effective mean chord length, $\bar{\Delta}_d$ is the mean detected chord length, p_u is the probability that a step point will not occur inside a pixel, and $\bar{\Delta}_u$ is the mean undetected chord length. These variables are a function of the path orientation relative to the reconstruction grid, described by the angle θ.

The explicit form of the effective mean chord length as a function of proton path orientation relative to the reconstruction grid (θ) is derived in the Appendix and is given as

$$\bar{\Delta}_{\text{eff}} = \frac{l}{3}\left(\frac{(s/l)^2 \sin 2\theta - 6}{(s/l)\sin 2\theta - 2(\cos \theta + \sin \theta)} \right.$$
$$\left. + \frac{(s/l)^2 \sin 2\theta}{2(\cos \theta + \sin \theta)} \right) \quad \text{for } 0° \leq \theta \leq 90°. \tag{6}$$

Here, l is the pixel size and s the step size. Due to symmetry of the square reconstruction grid, any path orientation can be rewritten as an angle between $0°$ and $90°$. In this work, a step size equal to half the pixel size was used. The effective mean chord length as a function of rotation angle is shown in Fig. 2.
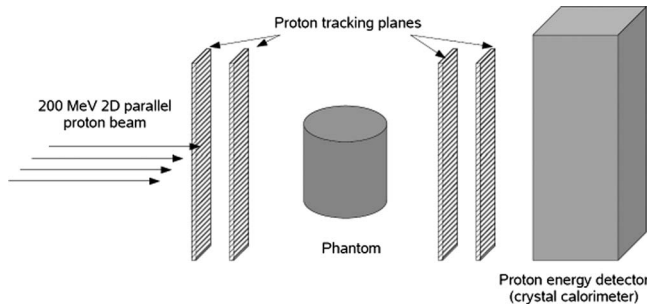
FIG. 3. Schematic of the GEANT4 simulation geometry used to model an ideal pCT system.

II.D. Proton CT simulation

To investigate the application of the different chord length approaches to reconstructed images, a GEANT4 (Ref. 15) simulation was carried out for a realistic pCT system, consisting of four proton tracking planes and a crystal calorimeter (Fig. 3). The incident proton beam consisted of a 200 MeV monoenergetic 2D parallel geometry. The $30 \times 30 \times 0.04$ cm^3 2D sensitive silicon tracking planes were assigned a spatial resolution of 100 μm. The calorimeter detector was a cesium iodide $32 \times 32 \times 10$ cm^3 rectangular prism with perfect energy resolution, i.e., sources of detector noise were neglected.

A cylindrical phantom with an elliptical cross section, based on the head phantom design of Herman,[16] was located at the center of the imaging system. The major axis of the phantom cross section was set to 17.25 cm and the minor axis to 13 cm. A cross section of the phantom can be seen in Fig. 4(a). The bone and bulk brain regions were assigned a
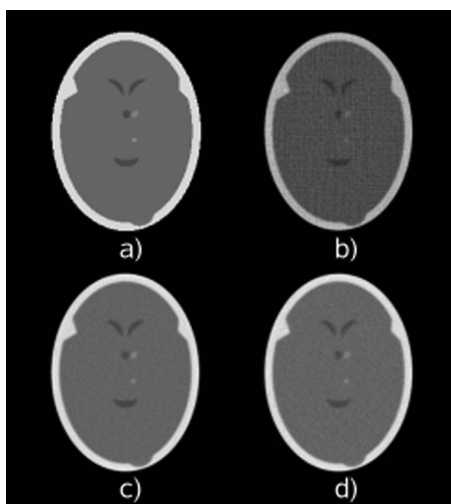
FIG. 4. (a) The Herman head phantom. Reconstructed images corresponding to the cycle of minimum relative error with (b) constant chord length, (c) exact chord length, and (d) effective mean chord length.

density and chemical composition corresponding to cranial bone and brain respectively, according to ICRP Report 23.[17] The ventricular regions (corresponding to cerebrospinal fluid) were assigned the chemical composition of water. All other structures had the chemical composition of brain but different densities.

The GEANT4 standard model for hadronic ionization was implemented with dE/dx values being calculated in 2000 bins ranging from 1 keV to 500 MeV, as suggested in Ref. 18. Elastic and inelastic nuclear collisions were also enabled. The first 20 000 proton histories to traverse the system and deposit energy in the CsI scintillator in each projection angle were recorded. A total of 180 projection angles at 2° intervals was carried out.

II.E. Proton CT image reconstruction and evaluation

For accurate MLP calculations,[8] the boundary of the imaged object is required to specify the region in which MCS can occur. To achieve this, an initial estimate of the image was found by processing the pCT data with an adaptation of the direct summation method, described in Ref. 19, prior to the iterative reconstruction. In this method, the proton path was simplified to a straight line and the backprojections of all line integrals [Eq. (1)] were summed. To obtain the boundaries from the resulting smooth image, a simple derivative-based filter[20] was used with a cutoff, to set the regions outside the object to 0.

Once the border of the object had been calculated, ART was used to find a solution to Eq. (3). The algorithmic structure of ART is

$$x^{k+1} = x^k + \lambda \frac{b_i - \langle a^i, x^k \rangle}{\|a^i\|^2} a^i. \tag{7}$$

Here, k is the iteration index, x^k and x^{k+1} are the current and updated image estimates, respectively, a^i is the i-th row vector of $\mathbf{A}$, b_i is as described above, and λ is a user determined relaxation parameter. A constant value of $\lambda = 0.002$ was used here, based on the results of previous work.[21] For a given reconstruction, 10 ART cycles were carried out, where a cycle refers to a complete execution of Eq. (7) for all proton indices i.

In this work, the analysis of image quality focused on quantitative accuracy of the relative stopping power values, as these values are most important for the accuracy of proton dose calculations. To compare reconstructed relative stopping powers to actual values, the phantom electron density was converted to a mean relative stopping power defined by

$$\rho_s = \frac{1}{\Delta E} \int_{10}^{200} \eta_{e,m}$$
$$\times \frac{[\ln(2m_e c^2 \beta^2(E)/(I_m(1-\beta^2(E)))) - \beta^2(E)]}{[\ln(2m_e c^2 \beta^2(E)/(I_{\text{water}}(1-\beta^2(E)))) - \beta^2(E)]} dE. \tag{8}$$

Here, $\eta_{e,m}$ and I_m are the electron density relative to water and mean excitation energy of the pixel, respectively. Note
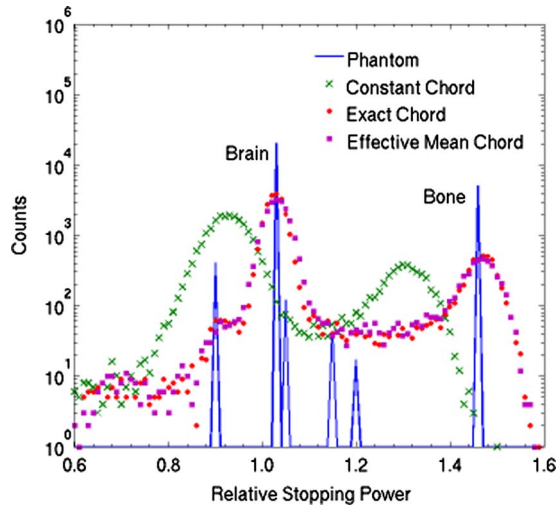
FIG. 5. Distribution of reconstructed relative stopping powers with constant chord length, exact chord length, and effective mean chord lengths.

that over the energy range of $\Delta E = 200 - 10$ MeV, the integrand varies only slowly with energy.

The relative error [Eq. (9)] of the reconstructed images after each cycle was calculated and used as a means of image quality evaluation,

$$\varepsilon_n = \sum_j |x'_j - x^n_j| / \sum_j |x'_j|. \tag{9}$$

Here, x'_j is the relative stopping power in pixel j of the phantom and x^n_j is the reconstructed relative stopping power in pixel j after n cycles.

III. RESULTS

III.A. Quantitative accuracy of proton CT reconstructions

The relative stopping power images of the smallest relative error within 10 ART cycles are shown in Fig. 4. Images reconstructed with a constant chord length equal to the pixel size [Fig. 4(b)], with an exact chord length [Fig. 4(c)], and effective mean chord length [Fig. 4(d)] are compared to the original phantom [Fig. 4(a)]. When the exact chord length or effective mean chord length approaches are used, image noise is considerably reduced.

Histograms of the relative stopping power values in the phantom and reconstructed images are shown in Fig. 5. The various anatomical regions (brain, bone, etc.) appear as peaks, which are broadened in the reconstructed images.

When a constant chord length is used, the relative stopping power values of all regions are systematically underestimated. Much closer agreement between the phantom and reconstructed values can be seen when an exact chord length or effective mean chord length method is used.

The peaks of the reconstructed brain and bone regions in Fig. 5 were fitted with a Gaussian function to quantify the accuracy of the various reconstruction approaches. The results are shown in Table I. The constant chord length approach displayed an approximate 10% underestimation of both brain and bone regions. This was reduced to 0.4% underestimation of the brain and 0.4% overestimation of the bone relative stopping powers when an exact chord length was used. The effective mean chord length approach displayed a brain peak position equivalent to the phantom, within statistical uncertainty, and overestimated the bone region by 0.3%. The standard deviations listed in Table I represent the amount of noise in the reconstructed images. The amount of noise is an important parameter for image quality as it determines the low-contrast density resolution of the images. Reconstructions with the exact chord length were found to display the least amount of noise.

III.B. Reconstruction time

Negligible difference in reconstruction time was found between the constant chord length and the effective mean chord length reconstruction. The exact chord length reconstruction was found to require approximately 20% more time for each reconstruction cycle.

IV. DISCUSSION

By using the energy loss and spatial tracking measurements of individual protons, pCT image reconstruction can provide the data required for proton treatment planning algorithms. Two methods for improving the accuracy of these reconstructions were described and tested in the current work. The first method generated a reconstruction system matrix consisting of exact chord lengths, by joining each MLP step point with a straight line segment. The second method assigned an effective mean chord length for all pixel intersections in a given proton history based on the orientation of the proton path relative to reconstruction grid.

It was found that reconstruction with both the exact chord length and the effective mean chord length resulted in better quantitative accuracy in comparison to the previously used constant chord length. With the new approaches, the relative stopping power of brain and bone regions was reconstructed

TABLE I. Results of a Guassian fit to histograms of reconstructed bone and brain regions in the relative stopping power images. The mean value with 95% confident limit and standard deviation σ are given.

Region	Phantom	Constant chord length		Exact chord length		Effective mean chord length	
		Mean	σ	Mean	σ	Mean	σ
Brain	1.031	0.926 ± 0.002	0.043	1.027 ± 0.001	0.020	1.031 ± 0.001	0.025
Bone	1.463	1.306 ± 0.001	0.046	1.469 ± 0.001	0.029	1.467 ± 0.003	0.034

to within 0.5% of the phantom values, effectively diminishing the substantial error of the constant chord length approach. However, bone values were still systematically overestimated. This can be explained by the fact that the current MLP formalism assumes *water* as the scattering medium. In bone regions, where the radiation length is less than water, the elements of the variance-covariance needed for the calculation of the MLP (Ref. 8) will be underestimated. This results in an underestimation of the MLP segment length that traverses bone, which, in turn, leads to overestimation of the relative stopping power. In order to comply with the observed energy loss, this overestimation must be compensated for elsewhere in the reconstruction, explaining the corresponding underestimation of brain regions.

In pCT, reconstructed image noise is generated through a combination of uncertainties in the proton path estimation, energy straggling within the imaged object, and noise in the energy detector measurements. In addition, the reconstruction algorithm can amplify the noise from these various sources. In the current work, the effect of proton path estimation was investigated with a GEANT4 generated pCT dataset that did not account for noise in the detector measurements. Since path estimation and detector noise are independent sources of noise, their respective variances will be additive. Thus, the same degree of improvement due to an improved proton path estimation approach can be expected in the presence of detector noise.

We demonstrated that image noise due to uncertainties in proton path estimation was reduced with both the exact chord length and the effective mean chord length approach in comparison to the images reconstructed with a constant chord length approach. Moreover, the exact chord length approach was found to display the least image noise. The additional noise in the effective mean chord length approach can be attributed to the assignment of one chord length value to each proton path, which is, of course, less accurate than calculating the exact chord length of the MLP for each pixel. The errors due to the assumption of a single path-grid orientation will be largest around 0° and 90°, where the rate of change in the effective mean chord length with orientation angle is largest (Fig. 2). However, considering the time saving advantages of approximately 20% per cycle with the effective mean chord length approach and the relatively minor difference in terms of noise, the effective mean chord length approach should be the preferred method in future pCT reconstruction studies.

V. CONCLUSION

Proton CT is an imaging modality that is capable of providing the data required for proton treatment plans in a more direct manner than the current x-ray CT approach. An exact chord length and an angle-dependent effective mean chord length were used to generate more accurate pCT reconstruction system matrices than the previously used constant chord length approach. The improvement in reconstruction accuracy was verified by reconstructing GEANT4 simulated pCT data with the ART algorithm. It was found that the error of
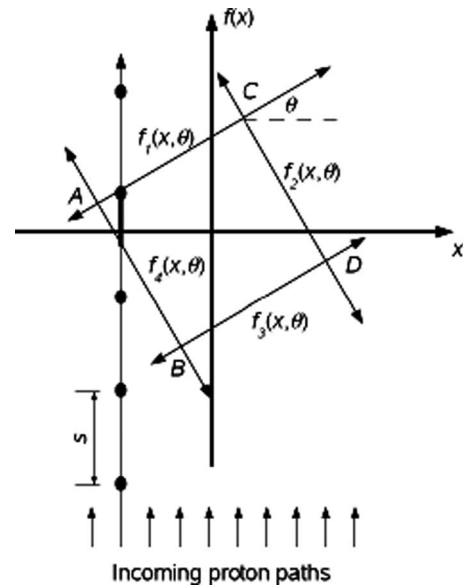
FIG. 6. Schematic of the rotated pixel geometry. The pixel vertices are denoted by points A, B, C, and D. The linear functions joining these points are labeled $f_1(x, \theta)$, $f_2(x, \theta)$, $f_3(x, \theta)$, and $f_4(x, \theta)$. A simplified straight line proton path is given as an example, illustrating the discrete stepping nature of the MLP. The step size is denoted by s. The chord length for this example is shown in bold.

approximately 10% in the mean reconstructed value for a given anatomical region, resulting from the previously used method, could be reduced to less than 0.5% with either of the new approaches. However, the considerable time saving advantages led us to conclude that the effective mean chord length approach was preferential for constructing pCT image reconstruction system matrices.

ACKNOWLEDGMENT

APPENDIX: DERIVATION OF THE EFFECTIVE MEAN CHORD LENGTH

To derive the functions describing the effective mean chord length, consider the representative pixel geometry illustrated in Fig. 6. Here, the rotated pixel vertices are denoted by points A, B, C, and D. Through coordinate rotation, the *x* component of these points for a pixel of size *l* can be calculated with

$$X_A(\theta) = -\frac{l}{2}(\cos \theta + \sin \theta),$$

$$X_B(\theta) = \frac{l}{2}(\sin \theta - \cos \theta),$$

$$X_C(\theta) = \frac{l}{2}(\cos \theta - \sin \theta),$$

$$X_D(\theta) = \frac{l}{2}(\cos\theta + \sin\theta). \tag{A1}$$

The linear functions of the pixel boundaries joining the vertices are labeled: $f_1(x,\theta)$, $f_2(x,\theta)$, $f_3(x,\theta)$, and $f_4(x,\theta)$. By using the point-gradient formula, the equation of each pixel boundary is given with

$$f_1(x,\theta) = x\tan\theta + \frac{l}{2\cos\theta},$$

$$f_2(x,\theta) = -\frac{x}{\tan\theta} + \frac{l}{2\sin\theta},$$

$$f_3(x,\theta) = x\tan\theta - \frac{l}{2\cos\theta},$$

$$f_4(x,\theta) = -\frac{x}{\tan\theta} - \frac{l}{2\sin\theta}. \tag{A2}$$

Approximating chords as straight lines, the chord length $\Delta(x,\theta)$ for all possible x values in the representative pixel is given by the piecewise function

$$\Delta(x,\theta) = \begin{cases} f_1(x,\theta) - f_4(x,\theta) & \text{for } X_A \le x \le X_B \\ f_1(x,\theta) - f_3(x,\theta) & \text{for } X_B \le x \le X_C \\ f_2(x,\theta) - f_3(x,\theta) & \text{for } X_C \le x \le X_D. \end{cases} \tag{A3}$$

Combining this with Eq. (A2), we have

$$\Delta(x,\theta) = \begin{cases} \dfrac{l(\cos\theta + \sin\theta) + 2x}{\sin 2\theta} & \text{for } X_A \le x \le X_B \\[3mm] \dfrac{l}{\cos\theta} & \text{for } X_B \le x \le X_C \\[3mm] \dfrac{l(\cos\theta + \sin\theta) - 2x}{\sin 2\theta} & \text{for } X_C \le x \le X_D. \end{cases} \tag{A4}$$

Due to the discrete stepping nature of the MLP procedure, the probability that a chord will be detected is unity when the chord length is greater than the stepping size s. When the chord length is less than the stepping size, the probability that the next step point will occur inside the pixel is given by the ratio of the chord length and the step size. Thus, the probability $[p_d(x,\theta)]$ of detecting a given chord requires the x locations x_{1e} and x_{2e}, at which the chord length is equal to the step size.

In Fig. 7, the derivation of x_{1e} is illustrated; due to symmetry, x_{2e} can be calculated in a similar manner. For a given step size s, x_{1e}, and x_{2e} are given by

$$x_{1e}(\theta) = X_A(\theta) + s\sin\theta\cos\theta,$$

$$x_{2e}(\theta) = X_D(\theta) - s\sin\theta\cos\theta. \tag{A5}$$

Therefore, in our notation the probability of a step point occurring within a pixel is given by the piecewise function
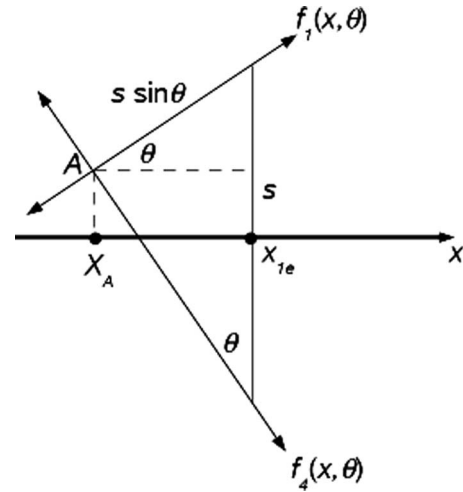
FIG. 7. Derivation of the point x_{1e} on the x axis at which the chord length through a pixel is equal to the step size s of the MLP procedure. Through symmetry, the same method can be used to derive x_{2e} for the positive x axis.

$$p_d(x,\theta) = \begin{cases} \dfrac{\Delta(x,\theta)}{s} & \text{for } X_A \le x < x_{1e} \\[3mm] 1 & \text{for } x_{1e} \le x \le x_{2e} \\[3mm] \dfrac{\Delta(x,\theta)}{s} & \text{for } x_{2e} \le x \le X_D. \end{cases} \tag{A6}$$

The mean detected chord length can now be calculated by taking a weighted average of chord lengths over all possible x values,

$$\bar{\Delta}_d(\theta) = \frac{\int_{X_A}^{X_D} p_d(x,\theta)\Delta(x,\theta)dx}{\int_{X_A}^{X_D} p_d(x,\theta)dx}. \tag{A7}$$

With the definitions of $\Delta(x,\theta)$ and $p_d(x,\theta)$ given by Eqs. (A4) and (A5), the explicit form of the mean detected chord length is given by

$$\bar{\Delta}_d(\theta) = \frac{l}{3}\left(\frac{(s/l)^2\sin 2\theta - 6}{(s/l)\sin 2\theta - 2(\cos\theta + \sin\theta)}\right). \tag{A8}$$

To derive the correction term, we require the probability that a step point does not occur inside the pixel p_u and the mean undetected chord length $\bar{\Delta}_u$. Firstly, p_u can be related to the probability of detection by

$$p_u(\theta) = 1 - \frac{\int_{X_A}^{X_D} p_d(x,\theta)dx}{X_D(\theta) - X_A(\theta)}. \tag{A9}$$

The mean undetected chord length [Eq. (A10)] is given by a weighted average in a similar manner to the mean detected chord length,

$$\bar{\Delta}_u(\theta) = \frac{\int_{X_A}^{X_D}(1 - p_d(x,\theta))\Delta(x,\theta)dx}{\int_{X_A}^{X_D}(1 - p_d(x,\theta))dx}. \tag{A10}$$

Combining these gives us the correction term

$$p_u(\theta)\bar{\Delta}_u(\theta) = \frac{l}{3}\left(\frac{(s/l)^2\sin 2\theta}{2(\cos \theta + \sin \theta)}\right). \qquad (A11)$$

Combination of Eqs. (A7) and (A11) results in the expression of the effective mean chord length given in Eq. (6) of the main text.

[a] Author to whom correspondence should be addressed. Electronic mail: snp75@uow.edu.au; Telephone: +61 4221 8194.

[1] P. L. Petti, "Differential-pencil-beam dose calculations for charged particles," Med. Phys. **19**, 137–149 (1992).

[2] L. Hong, M. Goitein, M. Gucciolini, R. Comiskey, B. Gottschalk, S. Rosenthal, C. Sergo, and M. Urie, "A pencil beam algorithm for proton dose calculations," Phys. Med. Biol. **41**, 1305–1330 (1996).

[3] G. T. Y. Chen, R. P. Singh, J. R. Castro, J. T. Lyman, and J. M. Quivey, "Treatment planning for heavy ion radio therapy," Int. J. Radiat. Oncol., Biol., Phys. **5**, 1809–1819 (1979).

[4] A. A. Mustafa and D. F. Jackson, "The relation between x-ray CT numbers and charged particle stopping powers and its significance for radiotherapy treatment planning," Phys. Med. Biol. **28**, 169–176 (1983).

[5] U. Schneider, E. Pedroni, and A. Lomax, "The calibration of CT Hounsfield units for radiotherapy treatment planning," Phys. Med. Biol. **41**, 111–124 (1996).

[6] B. Schaffner and E. Pedroni, "The precision of proton range calculations in proton radiotherapy treatment planning: Experimental verification of the relation between CT-HU and proton stopping power," Phys. Med. Biol. **43**, 1579–1592 (1998).

[7] R. W. Schulte, V. Bashkirov, T. Li, Z. Liang, K. Mueller, J. Heimann, L. R. Johnson, B. Keeney, H. F.-W. Sadrozinski, A. Seiden, D. C. Williams, L. Zhang, Z. Li, S. Peggs, T. Satogata, and C. Woody, "Conceptual design of a proton computed tomography system for applications in proton radiation therapy," IEEE Trans. Nucl. Sci. **51**, 866–872 (2004).

[8] R. W. Schulte, S. N. Penfold, J. T. Tafas, and K. E. Schubert, "A maximum likelihood proton path formalism for application in proton computed tomography," Med. Phys. **35**, 4849–4856 (2008).

[9] T. Li, Z. Liang, J. V. Singanallur, T. J. Satogata, D. C. Williams, and R. W. Schulte, "Reconstruction for proton computed tomography by tracing proton trajectories: A Monte Carlo study," Med. Phys. **33**, 699–706 (2006).

[10] H. Bethe, "Zur theorie des durchgangs schneller korpuskularstrahlen durch materie," Ann. Phys. **397**, 325–400 (1930).

[11] R. Gordon, R. Bender, and G. T. Herman, "Algebraic reconstruction techniques (ART) for three-dimensional electron microscopy and x-ray photography," J. Theor. Biol. **29**, 471–481 (1970).

[12] R. L. Siddon, "Fast calculation of the exact radiological path for a three-dimensional CT array," Med. Phys. **12**, 252–255 (1985).

[13] S. M. Stigler, "Thomas Bayes' Bayesian inference," J. R. Stat. Soc. Ser A (Gen.) **145**, 250–258 (1982).

[14] L. Eyges, "Multiple scattering with energy loss," Phys. Rev. **74**, 1534–1535 (1948).

[15] S. Agostinelli *et al.*, "GEANT4—A simulation toolkit," Nucl. Instrum. Methods Phys. Res. A **506**, 250–303 (2003).

[16] G. T. Herman, *Image Reconstruction from Projections: The Fundamentals of Computerized Tomography* (Academic, New York, 1980).

[17] International Commission on Radiological Protection, "*Report of the Task Group on Reference Man*," ICRP Publication 23 (Elsevier, Philadelphia, 1975).

[18] J. Heimann, L. Johnson, T. Satogata, and D. C. Williams, "The requirements and limitations of computer simulations applied to proton computed tomography," *IEEE NSS-MIC Conference Proceedings* (2004), pp. 3663–3666.

[19] G. T. Herman and S. W. Rowland, "Three methods for reconstructing objects from x-rays: A comparative study," Comput. Graph. Image Process. **2**, 151–178 (1973).

[20] R. Duda and P. Hart, *Pattern Classification and Scene Analysis* (Wiley, Hoboken, 1973).

[21] S. N. Penfold, R. W. Schulte, Y. Censor, V. Bashkirov, S. McAllister, K. E. Schubert, and A. B. Rosenfeld, in *Biomedical Mathematics: Promising Directions in Imaging, Therapy Planning and Inverse Problems*, edited by Y. Censor, M. Jiang, and G. Wang (Medical Physics, Madison, WI, in press).